ACCEPTED VERSION

Transparency and morphology control of Cu_2O photocathodes via an in-situ electro-conversion

*Marina Caretti, Linda Lazouni, Meng Xia, Rebekah A. Wells, Simon Nussbaum, Dan Ren, Michael Grätzel, Kevin Sivula**

Institute of Chemical Sciences and Engineering, Ecole Polytechnique Fédérale de Lausanne (EFPL), Station 6, CH-1015 Lausanne

Corresponding Author

*kevin.sivula@epfl.ch

ABSTRACT: Cu_2O is a model p-type semiconductor for photocathodes in photoelectrochemical (PEC) water splitting cells. However, major challenges remain in controlling its deposition into thin and homogeneous semi-transparent films. Herein, we report a new route to construct thin homogeneous Cu_2O layers on transparent fluorine doped tin oxide (FTO) substrates via the *in-situ* electro-conversion of CuSCN to Cu_2O. We highlight the morphology control of the resulting converted Cu_2O thin-films while demonstrating that they maintain promising performance for solar-driven hydrogen production with a maximum incident photon to current efficiency (IPCE) reaching 60% (at 0 V vs RHE and 450 nm) for a 180 nm-thick film and integrated solar photocurrents up to 4 mA cm^{-2}. In addition, altering the deposition conditions (e.g., applied potential, electrolyte compositions and pH) gives important insight into the mechanism and operation of the electro-conversion process.

TOC GRAPHICS

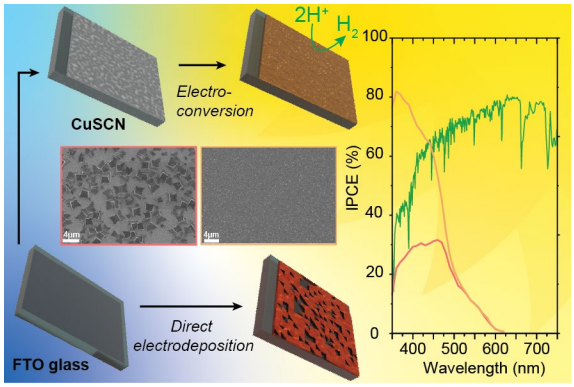

Developing efficient and economically-viable systems for the conversion of solar energy into chemical fuels is an important task towards a decarbonized economy.[1] Using photoelectrochemical (PEC) cells to directly split water into H_2 and O_2 is a promising method given the versatility of H_2 (e.g. as an energy storage vector and a chemical feedstock) and the relative simplicity of a PEC device.[2,3] A PEC tandem cell employs a photoanode and a photocathode to perform water oxidation and reduction, respectively, while also harvesting a significant portion of the solar spectrum, giving a maximum theoretical solar-to-hydrogen (STH) conversion efficiency over 20% under standard conditions.[4,5] Accordingly, the development of semiconductor materials that can meet performance requirements for cost-competitive PEC-based water splitting is an ongoing research goal.[6–9] Cuprous oxide, Cu_2O, is a promising candidate as a photocathode material due to its band gap energy (E_g = 2.0-2.1 eV), atomic abundance, and facile preparation by low-cost methods (e.g. electrodeposition[10]). As such, its ability to operate as the light-harvesting material in H_2-producing or CO_2/N_2 reducing photocathodes has been widely investigated.[11–15] Stabilized operation and water-reducing photocurrent densities close to the theoretical maximum for this material have been achieved by using electron transport layer (ETL) and protective over-layers (e.g. Ga_2O_3/TiO_2)[16–18] and nano/micro-structuring approaches,[19,20] respectively. However, in order to assemble a high-STH-efficiency PEC tandem cell, the Cu_2O photocathode should be used in a stack as the top cell given its E_g (while a photoanode with E_g = 1.2-1.5 eV would serve as the bottom cell).[5,21] Thus, control of the Cu_2O thickness and morphology is essential in order to tune light absorption and transmission.

Typically, Au-coated substrates are used to electrodeposit Cu_2O since this interface forms a low-resistance ohmic contact and also provides a suitable surface for the electrodeposition of Cu_2O, leading to homogeneous nucleation and good coverage. However, opaque Au substrates are not

suitable as the top-cell in a tandem configuration.[22] As such, alternative transparent underlayers for Cu_2O have been recently developed.[23,24] Nevertheless, electrodeposited Cu_2O generally results in the formation of micron-sized cubic crystals[25] that strongly scatter incident light. Since this light scattering can lead to significant losses in transmission to the bottom cell, as demonstrated with Cu_2O[26] and other oxide semiconductor photoelectrodes,[27] there remains a general need to develop methods to control the morphology and transparency of Cu_2O formed by electrodeposition. This is especially important for the application of Cu_2O in extremely-thin-absorber type photoelectrodes, where a large surface area conductive template is coated with an ultrathin Cu_2O layer. While promising performances have been obtained with Cu_2O grown on an opaque Cu 3D-network,[28,29] the demonstration of a highly photo-active ultrathin (< 200 nm) Cu_2O layer electrodeposited on transparent conductive substrates has not been yet achieved.

Herein we report that electrodeposited CuSCN can be used as precursor for the electro-conversion into Cu_2O under specific electrochemical conditions. Our discovery resulted from work on the CuSCN/Cu_2O heterojunction, which has been established in photocathodes[24,30] and in photovoltaic devices.[31] However, our efforts to investigate conditions for the subsequent electrodeposition of Cu_2O on CuSCN led to the surprising observation of an electro-conversion process. We show that the electro-conversion allows for a novel morphological control of Cu_2O film on transparent conductive substrates and we further investigate the key parameters required to drive the *in-situ* CuSCN electro-conversion. Finally, we highlight the optoelectronic and photoelectrochemical advantages of the converted Cu_2O photocathode over the direct deposition on transparent substrates.

Following common procedures (see experimental methods section) a layer of CuSCN was first electrodeposited on transparent F-doped SnO_2 (FTO) coated glass substrates using a constant

applied potential of –0.3 V vs Ag/AgCl with a $CuSO_4$ and KSCN-based electrolyte. The resulting layer exhibits a nanopillar structure (see scanning electron micrograph, SEM, images Figure S1, Supporting Information, SI) and the crystal structure is verified by X-Ray diffraction (XRD), as shown in Figure S2, SI. The thickness can be tuned by varying the deposition time with a 2-min and 10-min electrodeposition leading to thicknesses of 140 nm and 570 nm, respectively (see cross-sectional SEM Figure S1, SI). During the subsequent electrodeposition of Cu_2O with a copper(II) lactate complex, but using a higher pH of 12 compared to previous work,[24] an interesting behavior is observed during constant-current electrodeposition as shown by chronopotentiometry (–0.1 mA cm^{-2}) in Figure 1 for electrodeposition on bare FTO glass compared to thick (570 nm) or thin (140 nm) layers of CuSCN on FTO.

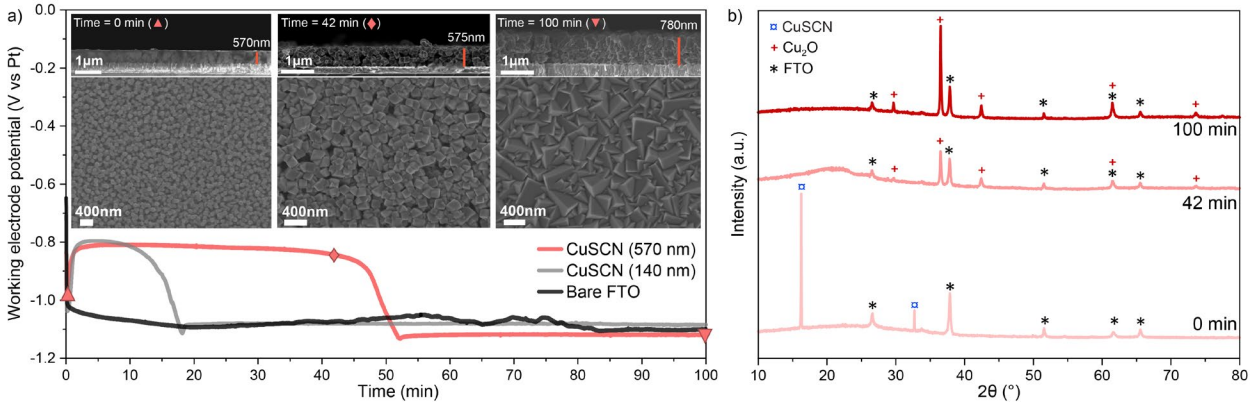

Figure 1. (a) Potential evolution during Cu_2O electrodeposition by chronopotentiometry at –0.1 mA cm^{-2} on bare FTO, and FTO/CuSCN substrates with different thicknesses of CuSCN. SEM images (top-view and cross section) are shown in the insets for the FTO/CuSCN (570 nm) substrate at various times during the electrodeposition (0, 42, and 100 min) and the corresponding points on the chronopotentiometry curve are indicated. (b) XRD patterns of 570 nm CuSCN film during *in-situ* electro-conversion at time = 0 min, 42 min and 100 min.

For the same current density during the electrodeposition (–0.1 mA cm^{-2}), the potential evolves differently for bare FTO and CuSCN/FTO substrates. When bare FTO is used, the potential remains constant at ca. –1.1 V vs Pt during a 100 min deposition. However, a less negative

potential (–0.8 V) is initially observed for CuSCN-coated FTO followed by a shift to –1.1 V at around 15 and 48 min for the thin (140 nm) and thick (570 nm) CuSCN substrates, respectively. The obvious correlation between the duration of the less negative potential segment of the deposition to the thickness of the CuSCN layer suggests a process involving the CuSCN is occurring during the low potential phase of the deposition. In order to gain insight into this process, we examined the morphology of the substrate at different deposition times in the thick CuSCN layer case as shown by top-down and cross-sectional SEM image insets in Figure 1a. Before the electrodeposition (time = 0) the substrate is composed of the typical CuSCN nanorods with a thickness of 570 nm as expected. Interestingly, at time = 42 min, before the shift in potential, the rounded CuSCN nanorods seem to have changed shape, appearing more cubic with a size of 100-200 nm; however, the thickness of the film remains largely unchanged. Continuing the electrodeposition after the potential shift, at t = 100 min, the thickness of the resulting film increases to 750 nm and the typical micron-sized cube morphology of electrodeposited Cu_2O is observed on the top of the small-cube layer. XRD of the 0, 42, and 100-minute samples (Figure 1b) show the dominant peaks of Cu_2O at 2θ = 29.6, 36.5, 42.3, 61.4 and 73.5° corresponding to the (110), (111), (200), (220), (311) planes[32] emerging after 42 min and becoming more intense after 100 min while the characteristic (003) CuSCN peak is already absent after 42 min. X-ray photoelectron spectroscopy (XPS) further confirms the total transformation of CuSCN to Cu_2O (Figure S3, SI). Indeed, neither sulfur nor nitrogen was detected in the Cu_2O prepared from the CuSCN layer, in contrast to the original CuSCN film (Figures S3a,b). The Cu 2p 3/2 signal exhibits two features at 932.5 and 934.5 eV (Figure S3c). The 932.5 eV signal cannot be attributed to Cu^0 considering the fit of the LMM auger transition spectrum (Figure S3d) using the Biesinger method.[33] The peak at 934.5 eV is attributed to $Cu(OH)_x$ species present due to air exposure of the

Cu_2O surface, therefore it is not present in the CuSCN sample. Moreover, energy-dispersive X-ray (SEM-EDX) mapping obtained in analytic mode (Figure S4, SI) shows only copper (Cu), oxygen (O), element signals, and no sulfur signal (no peak at 2.307 keV) indicating the complete transformation of CuSCN to Cu_2O.Overall, the SEM, EDX, XRD,XPS results support the view that the CuSCN layer can be converted to Cu_2O during electrodeposition at pH 12. Furthermore, the chronopotentiometry results suggest that the electro-conversion of CuSCN to Cu_2O occurs at a potential of –0.8 V vs Pt.

In order to identify the parameters essential for driving the formation of Cu_2O via the observed *in-situ* electro-conversion of CuSCN, and to gain insight into the transformation mechanism, we performed additional experiments by varying the processing conditions. First, to understand the importance of the pH on the stability of the CuSCN layer we investigated the impact of a 1-min dipping of an FTO/CuSCN film in copper lactate-based electrolyte at different pH (without any applied potential). As shown in Figure S5, SI, at pH 12 the CuSCN (003) XRD peak is still present, however the shape and density of the CuSCN nanopillars are slightly changed. This change is more intense at pH 13 than pH 12. Indeed, at pH 13, the FTO substrate is partially visible via top-view SEM (Figure S5c), and the (003) CuSCN XRD peak vanishes, suggesting that the CuSCN is dissolved/corroded in the electrolyte under these conditions. However, we also observed weak reflections of Cu_2O or $Cu(OH)_2$ on the XRD spectra (Figure S5d), which become more intense at pH 13 compared to pH 12. Furthermore, photographs of the films (Figure S6, SI) show a color change occurring during the dipping process, from the typical colorless CuSCN to a yellowish film, when FTO/CuSCN substrates are dipped in pH 12 or 13 electrolyte while at pH 11 the film does not change. Thus, we conclude that at pH $\geq$ 12 the CuSCN layer can undergo dissolution and conversion to a highly amorphous phase, likely based on a Cu_2O or Cu(OH) stoichiometry. Indeed,

the formation of a Cu_2O-$Cu(OH)_2$ nanocomposite has been suggested to form in alkaline media when using CuSCN as precursor[34], confirming the possibility of CuSCN conversion. However, in our experiments there is no evidence of the full conversion to $Cu(OH)_2$ or Cu_2O This can be explained by the presence of lactate ion which complexes Cu^{2+} ions and likely leads to the dissolution of the CuSCN. In fact, after a prolonged dipping time the material at the surface of the FTO glass is completely dissolved for both pH 12 and pH 13 (Figure S6).

The importance of the presence of the copper ion in the electrolyte is further illustrated in Figure S7, SI, where XRD and SEM images of FTO/CuSCN films are shown after 1-min dipping in electrolyte at pH 12 without Cu^{2+}. In the case without both copper and lactate (pH 12 adjusted with NaOH) the density of the CuSCN nanorods decreases and some needle-like structures are formed, while in electrolyte without Cu ions but with lactate, the nanorods are slightly dissolved as some small pores can be observed. For both cases some weak Cu_2O or Cu(OH) reflections appear in the XRD spectra at 36° and 42° (for dipping in NaOH). The latter result suggests that the Cu ions are not essential for the phenomenon to take place without applied potential. However, comparing the results from Figures S6 and S7, the presence of lactate in the solution appears to be key to control the morphology. Overall, with the dipping experiments, we can conclude that the formation of Cu_2O pure films cannot arise from a simple solid-liquid reaction, as the cathodic polarization seems to be crucial for the transformation to occur.

While it is clear that applying a cathodic current is necessary to afford the CuSCN conversion to Cu_2O, it is also important to note that the electrolyte composition plays a role in the electro-conversion. This is illustrated by additional electrodeposition experiments in pH 12 electrolyte without Cu ions (Figure S8, SI). In both cases of electrolyte with or without lactate, after 100 min of chronopotentiometry at -0.1 mA cm^{-2}, solely weak Cu_2O XRD peaks are visible at 42°.

Likewise the preceding dipping experiment, these minor traces are not comparable to the cubic Cu_2O layer obtained with typical Cu_2O electrodeposition electrolyte (Cu ions, lactate, K_2SO_4), in Figure 1. Rather the CuSCN nanopillars are transformed into amorphous structures. The applied potential is also found to affect the conversion, as shown by performing the electrodeposition in copper lactate electrolyte (pH 12) at different potentials ranging from –0.1 V to –1.1 V (vs Pt) for a 100-min deposition on an FTO/CuSCN substrate. In Figure S9, SI, we can see that at –0.1 V, the conditions are not sufficiently negative to drive the transformation; the CuSCN is almost totally dissolved. The same conclusion can be made at –0.5 V, however the dissolution seems slower as more CuSCN nanorods are visible by SEM after 100 min. At the more negative potential of –0.8 V, which is the typical potential for a Cu_2O chronopotentiometry deposition (see Figure 1), the substrate surface is fully covered with Cu_2O. Thus, we conclude that both the proper electrolyte (copper and lactate ions at pH ≥ 12) and a sufficiently negative potential must be applied to drive the *in-situ* electro-conversion.

Further insight is gained into the mechanism of the electro-conversion by comparing Cu_2O films prepared by the two methods shown in Figure 2a. The "Cu_2O_D" film is grown directly on bare FTO and "Cu_2O_C" is prepared via CuSCN electro-conversion, terminating just as the conversion transitions to the standard electrodeposition (which is easily monitored via the potential during the deposition). A 180 nm thick-film of CuSCN (corresponding to 25 mC cm^{-2} of charge passed during the CuSCN electrodeposition) was used to prepare the Cu_2O_C film. For both the Cu_2O_C and Cu_2O_D films, the Cu_2O film was deposited at -0.1 mA cm^{-2} for 20 min (120 mC cm^{-2}). The morphology difference between the Cu_2O prepared by the two routes is shown in the SEM images in Figure 2b-g. While the Cu_2O_C film is evenly coated (has an FTO coverage of 100%) the coverage is incomplete for the Cu_2O_D film and is estimated at 46% by inspection of the SEM

images. The absence of a favorable back contact such as gold for the Cu_2O_D sample can explain the uneven coverage. It should be noted that by increasing the deposition time for the Cu_2O_D film, the surface becomes increasingly covered (Figure S10, SI). However, after 90 min the coverage is still not 100%.

In addition to substrate coverage, the cube size and the film thickness are different for the two preparation routes (keeping the same deposition current of 120 mC cm^{-2}): the cube edge length is 300-400 nm and 1.5-2 µm for Cu_2O_C and Cu_2O_D, respectively, while the average film thickness is around 180 nm and 400 nm, respectively. Consistent with our observations in Figure 1, the thickness of the film remains the same during the electro-conversion. Considering the density of CuSCN and Cu_2O are, respectively, 2.8 and 6.0 g cm^{-3}, it appears that the mass of the film doubles during the *in-situ* electro-conversion. Moreover, despite the fact that the Cu_2O_C sample passes more current during the electrodeposition (25 mC cm^{-2} during the CuSCN deposition plus 120 mC cm^{-2} during the electro-conversion), both electrodes appear to contain similar amounts of Cu_2O. Indeed, comparing the coverage of the Cu_2O_D film (46%) and its average thickness of 400 nm suggests an amount of Cu_2O equivalent to a 180 nm-thick continuous film, which is the same as for the Cu_2O_C film (see below UV-vis data for further support). Since CuSCN already contains Cu(I) it could be reasonable to consider that only one Cu(II) ion from the electrolyte needs to be reduced and incorporated into the converting CuSCN film to give Cu_2O. This does not appear to be the case. Indeed, considering the constant film thickness together with the different densities of CuSCN and Cu_2O and the observations of the dissolution of the CuSCN upon exposure to pH 12 without the applied potential suggest a mechanism wherein the dissolution of the CuSCN occurs during the electrodeposition of Cu_2O. As Cu_2O is thermodynamically stable at pH 12 at the applied potential, it results in the deposition of Cu_2O cubes. We suggest that the CuSCN acts as an

intermediate—reducing the required potential to deposit the Cu_2O and acting as a morphological template, leading to the smaller cube size observed in the Cu_2O_C films. However, additional investigation is needed to fully elucidate the complex reduction mechanism occurring during the electro-conversion process.

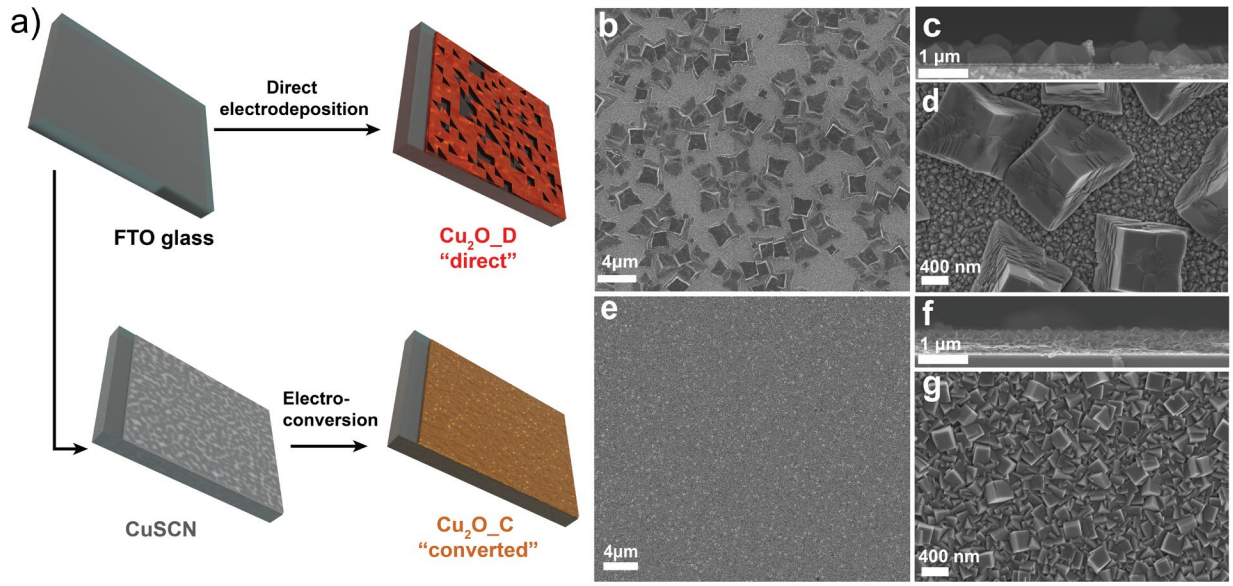

Figure 2. (a) Schematic of the possible routes to make Cu_2O by direct Cu_2O electrodeposition (Cu_2O-D) and by CuSCN electrodeposition followed by *in-situ* electro-conversion to Cu_2O (Cu_2O-C), (b-g) SEM images of (b-d) Cu_2O_D direct deposition (e-g) Cu_2O_C converted film.

Nevertheless, given the distinct morphology differences between the Cu_2O formed by the electro-conversion method, with smaller sized nanocubes and smoother crystal facets (with apparently fewer defects compared to the traditional electrodeposition directly on FTO, see additional SEM images Figure S11, SI), we speculated that the electro-converted films would offer higher transparency and improved photocathode performance compared to the standard deposition on bare FTO. To assess this and further characterize the converted CuSCN samples, we performed UV-Visible spectroscopy, Raman spectroscopy, and XRD on the films. Figure 3a shows the

Raman spectra of Cu_2O_D and Cu_2O_C where the typical Cu_2O resonance peaks between 100-250 cm^{-1} are seen in both cases. Similarly, the XRD analysis in Figure 3b shows nearly identical diffraction patterns with Cu_2O peaks at 2θ = 29.6, 36.5, 42.3, 61.4 and 73.5° corresponding to the (110), (111), (200), (220), (311) planes. The smaller crystallinity in the Cu_2O_C films is evident by increased full width at half maxima (FWHM). However, the optical properties are quite different as evident from the photographs of the films (Figure 3a, inset) and the total absorptance and direct transmittance spectra (Figure 3c). Both samples have an absorption onset around 600 nm, typical for Cu_2O, and a similar absorptance at 550 nm—further suggesting that both films have the same amount of Cu_2O deposited, as suggested above. We verified this by calculating the theoretical absorptance of the Cu_2O_D film taking into account the film coverage, average thickness and the Cu_2O absorption coefficient[35] at 550 nm (See SI, theoretical calculation). We estimate an absorptance of 20%, which is on good agreement to the measured value (21%). The difference between the Cu_2O_D and Cu_2O_C films at shorter wavelengths is attributed to the increase of the absorption coefficient, the coverage of the Cu_2O, and the morphology of the Cu_2O cubes. Indeed, the absorptance of the Cu_2O_D film is lower at wavelengths smaller than 500 nm due to the direct passing of photons through the uncoated parts of the FTO surface. The incomplete coverage and large crystal size of the Cu_2O_D film also leads to more light loss by scattering. The direct transmittance is around 50-70% in the range 600-900 nm for Cu_2O_C, while it is only 30% for Cu_2O_D. Thus, the Cu_2O_C samples exhibit higher transparency for non-absorbed photons despite the full surface coverage.

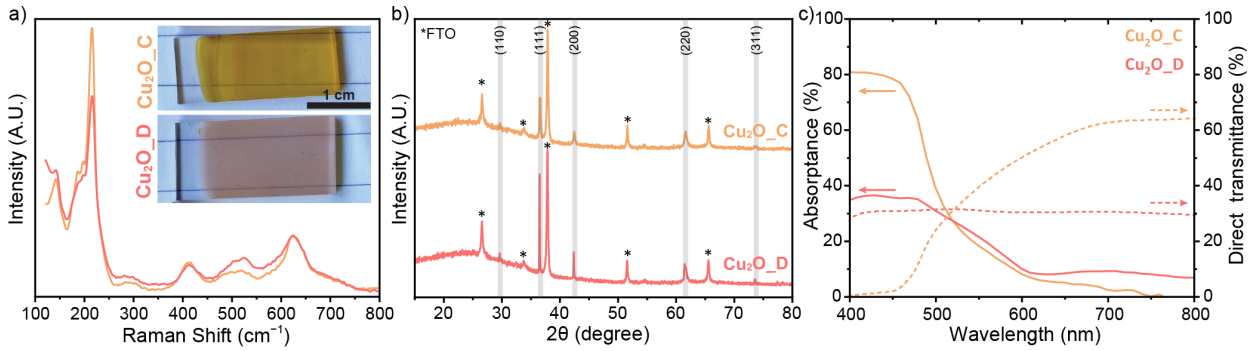

Figure 3. Characterization of thick Cu_2O films obtained by direct deposition (Cu_2O_D) and by the *in-situ* electro-conversion (Cu_2O_C): (a) Raman spectra (inset) photograph of the electrodes (b) XRD spectra (c) UV-visible total absorptance and direct transmittance spectra.

In order to establish the ability of the electro-converted Cu_2O to perform as a photocathode for H_2 production, we fabricated complete photoelectrodes by adding protective and co-catalyst layers following the route established by Pan et al.[20] (Ga_2O_3/TiO_2 by ALD and RuO_2 catalyst by photoelectrodeposition[36]). We compared the HER performance with linear scanning voltammetry (LSV) under intermittent (simulated) solar illumination of the Cu_2O_D and Cu_2O_C photoelectrodes described in Figures 2 and 3 (with approximately the same amount of Cu_2O). The LSV curves are shown in Figure 4a.

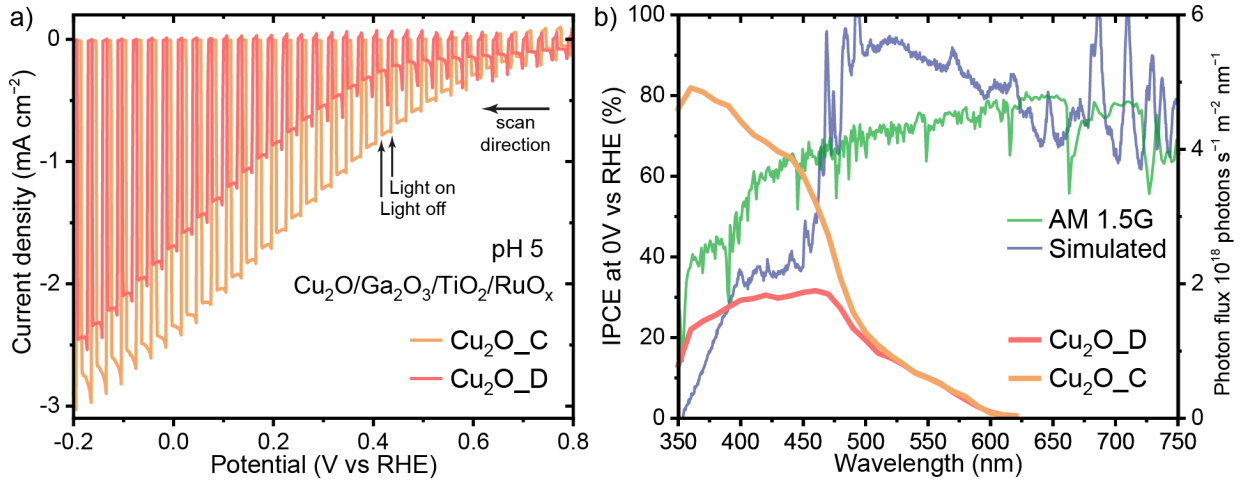

Figure 4. (a) Linear scanning voltammetry of Cu_2O-based photocathodes for H_2 production under intermittent simulated solar illumination (1 sun) LSV at pH 5 for HER. (b) IPCE spectra of the Cu_2O photocathodes at 0V vs RHE at pH 5 are shown next to the standard solar spectrum (green) and the simulator solar spectrum produced by the light source used during the LSV tests (blue).

In terms of photocurrent density, higher performance was obtained for Cu_2O_C (2.5 mA cm^{-2} at 0 V vs RHE) compared to Cu_2O_D (2 mA cm^{-2} at 0 V vs RHE) under simulated 1 sun illumination. The qualitatively higher fill-factor of the LSV curve in the Cu_2O_C photocathode suggests that the semiconductor layer benefits from an improved electrical contact to the FTO substrate compared to the Cu_2O_D photocathode. While using CuSCN as an underlayer is known to improve the contact with the substrate, it is notable that a similar improvement is seen with the electro-converted film, despite no detectable CuSCN remaining in the film.

Incident photon-to-current efficiency (IPCE) measurements, taken with monochromatic light at 0 V vs RHE further highlight the performance difference between converted and direct depositions (Figure 4b). While the IPCE for both cases is similar in the wavelength range from 500-600 nm, due to the similar light absorption in this region, Cu_2O_D exhibits lower IPCE for wavelengths < 500 nm due to the incomplete film coverage. Specifically, the IPCE at 450 nm is 32% and 60% for Cu_2O_D and Cu_2O_C, respectively. The IPCE of the Cu_2O_C photocathode reaches 80% at 350 nm, which, together with the measured absorptance at that wavelength, suggests an internal quantum efficiency of close to 100% under these conditions. Integration of the IPCE data with the standard solar spectrum (Figure 4b, green trace) gives an estimated photocurrent density of 4.0 mA cm^{-2} at 0 V vs RHE with the Cu_2O_C photocathode compared to 2.4 mA cm^{-2} for the Cu_2O_D

photocathode (See Figure S12, SI) confirming the improved performed of the Cu_2O_C. The discrepancy between the photocurrent measured under simulated solar conditions in Figure 4a and the predicted solar photocurrent from the IPCE measurements is attributed to the deficiency of UV photons in the solar simulator employed for the LSV measurements (see blue trace in Figure 4b). This difference together with the fact that the Cu_2O_C photocathode shows a linear response of photocurrent to light intensity (See Figure S13, SI) indicates that the integrated IPCE results give a more accurate estimation of the true solar photocurrent. Overall, given the considerable difference in photocathode performance in the 350-500 nm range, and the drastically improved transmittance of the Cu_2O_C layer in the 550-800 nm range (as shown in Figure 3c) compared to the availability of solar photons in this wavelength range, we conclude that the Cu_2O_C films are well-suited for the coating of high surface transparent scaffolds or as top cells in tandem devices for overall water splitting. The exploitation of these prospects is under development in our lab.

To conclude, we have demonstrated a novel method to control Cu_2O thin film morphology for semi-transparent photocathode applications. By first electro-depositing a nanostructured CuSCN layer and then electro-depositing Cu_2O under specific conditions, the CuSCN acts as a sacrificial template and catalyst to lower the required potential for Cu_2O deposition. This electro-conversion process allows homogeneous Cu_2O coverage on transparent FTO substrates while similar deposition directly on the FTO gives inhomogeneous film with poor transparency due to light scattering. Control experiments revealed that key parameters are essential for the *in-situ* electro-conversion: pH $\geq$ 12 electrolyte containing Cu-lactate complexes and the application of a sufficiently negative current/potential. By comparing films with similar amounts of Cu_2O, we found that the photocathode performance (for H_2 evolution) of electro-converted Cu_2O (Cu_2O_C)

was superior to Cu_2O films directly deposited on the FTO (Cu_2O_D), due to improved substrate interaction and higher quantum efficiencies at low wavelengths. Thus, the Cu_2O deposition by electro-conversion is a promising alternative to coat homogenous and thin Cu_2O layer without scattering losses and without compromising the transparency of the electrode.

Experimental methods

Chemicals. Copper(II)sulfate pentahydrate $CuSO_4,5H_2O$ (99% Acros organics), Ethylenediamintetraacetic acid $C_{10}H_{16}N_2O_8$ (99% Acros organics), Potassium thiocyanate KSCN (99% Acros organics), Potassium sulphate K_2SO_4 (99% Carl ROTH), DL-lactic acid (90% abcr), Potassiumhydroxide KOH (pure Reactolab), Sodium sulfate $NaSO_4$ (99% Sigma aldrich), Potassium phosphate, monobasic, KH_2PO_4 (99% Acros organics), Sodium hydroxide NaOH (pure Reactolab) and Potassium perruthenate $KRuO_4$ (98% strem chemicals) were used as received.

CuSCN deposition. FTO glass (2.5 cm × 1 cm) were cleaned with detergent (20 min), water (20 min), IPA (20min). CuSCN is deposited following a procedure developed elsewhere.[24] Briefly, CuSCN electrodeposition is performed in an aqueous solution containing 12mM of $CuSO_4$, EDTA and KSCN added in this specific order to order to avoid the precipitation of $Cu(SCN)_2$. A standard three-electrode configuration was used for electrochemical deposition with Pt counter electrode and Ag/AgCl/sat. KCl reference electrode. Chronoamperometry at –0.3 V vs Ag/AgCl is applied for a defined duration/charge passed. In the potential drop experiment (Figure 1) thin and thick film correspond to an electrodeposition time of 2 and 10 min. For the rest of the study, in order to

keep the amount of CuSCN deposited constant for each condition, thin CuSCN and thick CuSCN correspond to a charge passed of 50 mC and 100 mC respectively.

Cu_2O photocathode formation. Cu_2O films were deposited on bare FTO (Cu_2O_D) or on CuSCN (Cu_2O_C) with method developed elsewhere[16]. Cu_2O was electrodeposited in a copper-lactate rich electrolyte at pH 12. The electrolyte contains 4 g of $CuSO_4$,$5H_2O$, 33.8 g of Lactic acid, and 10.9 g of K_2SO_4 in 250 mL of DI water. The pH was adjusted to 12 by adding 2 M KOH. The final volume of the electrolyte is 500 mL. A large piece of platinum was used as a counter electrode. The electrodeposition is performed by chronopotentiometry at a current density of –0.1mA cm^{-2}. The temperature was maintained at 30°C using a water bath. Deposition time was varied depending on the film thickness expected. For *in-situ* electro-conversion on CuSCN, the chronopotentiometry was started just after sample immersion in the electrolyte to avoid CuSCN dissolution. 20 nm of Ga_2O_3 and 20 nm of TiO_2 layers were deposited on the Cu_2O film using a Savannah 100 (Cambridge Nanotech) thermal ALD system. The chamber was stabilized at 150°C and flushed with 10 sccm nitrogen gas (99.9995%, Carbagas). Gallium oxide was deposited using bis(μdimethylamino)tetrakis(dimethylamino)digallium (98%, Stream Chemicals) and TiO_2 was deposited using tetrakis(dimethylamino)titanium (99.999%, Sigma). RuO_x catalyst was photoelectrodeposited by chronopotentiometric method at 28 μA cm^{-2} under illumination in presence of 1.3 mM $KRuO_4$ aqueous solution for 5min. Pt wire was used as counter electrode.

Material characterization. UV-Visible spectrometry was performed with a UV-3600 (Shimadzu) spectrometer equipped with an integrating sphere. Bragg-Brentano XRD measurements were carried out using a Bruker D8 Vario diffractometer equipped with a Johansson Kα1 (λ = 1.5406 Å). SEM images were recorded with a Zeiss Merlin microscope. Raman spectra were obtained with a LabRam spectrometer (Jobin Yvon Horiba). The excitation line was provided

by an argon laser (532.19nm). XPS measurements were carried out on an Axis Supra (Kratos Analytical) instrument, where a monochromated Kα X-ray line of an aluminum anode was used. The pass energy was set to 20 eV with a step size of 0.1 eV. The samples were grounded to the sample holder by connecting the FTO underlayer to the sample stage.

Photoelectrochemical characterization. PEC experiments were performed by using a three-electrode setup, with carbon rod as counter electrode and Ag/AgCl/KCl sat as reference electrode. Pec performances were measured in a pH 5 buffer solution containing 0.5M Na_2SO_4, 0.1 M sodium phosphate. The surface area of the film is contact with the electrolyte was in the range 0.1-0.2 cm^2. The electrochemical behavior was monitored with a SP-200 potentiostat (biologic), while the light was provided by a xenon arc lamp (450W) calibrated with the AM 1.5G spectra to provide one sun of illumination (1000 mW cm^{-2}). A mechanical shutter was used to chop the light. All experiments were carried out at ambient temperature and electrode potentials were converted to the RHE scale using $E_{RHE} = E_{Ag/AgCl} + 0.059\ pH + 0.197$. Incident photon to current efficiencies (IPCE) were obtained using an Optical Building Blocks Corporation tunable PowerArc illuminator for illumination where the photon flux was calibrated with a Thorlabs Model S120VC Photodiode Power Sensor. The photocurrent was recorded in the same three-electrode potentiostatic configuration described above at 0 V vs RHE. The working electrodes were illuminated from the substrate side in all cases.

ASSOCIATED CONTENT

Supporting Information. The Supporting Information is available free of charge at:

Additional SEM images, XRD plots, XPS spectra, sample photographs, integrated photocurrent data, and photocurrent linearity as described as Figures S1-S13 in the main text as well and extended experimental data on the theoretical absorptance calculation (PDF)

AUTHOR INFORMATION

Corresponding Author

Kevin Sivula − Institute of Chemical Sciences and Engineering, Ecole Polytechnique Fédérale de Lausanne (EFPL), Station 6, CH-1015 Lausanne ; orcid.org/0000-0002-8458-0270;

Email: kevin.sivula@epfl.ch

Notes

The authors declare no competing financial interest.

ACKNOWLEDGMENT

This project has received funding from the European Union's Horizon 2020 research and innovation program under grant agreement No 883264. The authors thank P. Schouwink and M. Mensi for assistance with XRD and XPS.

REFERENCES

(1) Davis, S. J.; Lewis, N. S.; Shaner, M.; Aggarwal, S.; Arent, D.; Azevedo, I. L.; Benson, S. M.; Bradley, T.; Brouwer, J.; Chiang, Y.-M.; Clack, C. T. M.; Cohen, A.; Doig, S.; Edmonds, J.; Fennell, P.; Field, C. B.; Hannegan, B.; Hodge, B.-M.; Hoffert, M. I.; Ingersoll, E.; Jaramillo, P.; Lackner, K. S.; Mach, K. J.; Mastrandrea, M.; Ogden, J.; Peterson, P. F.; Sanchez, D. L.; Sperling, D.; Stagner, J.; Trancik, J. E.; Yang, C.-J.; Caldeira, K. Net-Zero Emissions Energy Systems. *Science* **2018**, *360* (6396), eaas9793. https://doi.org/10.1126/science.aas9793.

(2) Kim, J. H.; Hansora, D.; Sharma, P.; Jang, J.-W.; Lee, J. S. Toward Practical Solar Hydrogen Production – an Artificial Photosynthetic Leaf-to-Farm Challenge. *Chem. Soc. Rev.* **2019**, *48* (7), 1908–1971. https://doi.org/10.1039/C8CS00699G.

(3) Sivula, K.; van de Krol, R. Semiconducting Materials for Photoelectrochemical Energy Conversion. *Nat. Rev. Mater.* **2016**, *1* (2), 15010. https://doi.org/10.1038/natrevmats.2015.10.
(4) Pinaud, B. A.; Benck, J. D.; Seitz, L. C.; Forman, A. J.; Chen, Z.; Deutsch, T. G.; James, B. D.; Baum, K. N.; Baum, G. N.; Ardo, S.; Wang, H.; Miller, E.; Jaramillo, T. F. Technical and Economic Feasibility of Centralized Facilities for Solar Hydrogen Production via Photocatalysis and Photoelectrochemistry. *Energy Environ. Sci.* **2013**, *6* (7), 1983–2002. https://doi.org/10.1039/C3EE40831K.
(5) Prévot, M. S.; Sivula, K. Photoelectrochemical Tandem Cells for Solar Water Splitting. *J. Phys. Chem. C* **2013**, *117* (35), 17879–17893. https://doi.org/10.1021/jp405291g.
(6) Yao, T.; An, X.; Han, H.; Chen, J. Q.; Li, C. Photoelectrocatalytic Materials for Solar Water Splitting. *Adv. Energy Mater.* **2018**, *8* (21), 1800210. https://doi.org/10.1002/aenm.201800210.
(7) He, Y.; Hamann, T.; Wang, D. Thin Film Photoelectrodes for Solar Water Splitting. *Chem. Soc. Rev.* **2019**, *48* (7), 2182–2215. https://doi.org/10.1039/C8CS00868J.
(8) Lumley, M. A.; Radmilovic, A.; Jang, Y. J.; Lindberg, A. E.; Choi, K.-S. Perspectives on the Development of Oxide-Based Photocathodes for Solar Fuel Production. *J. Am. Chem. Soc.* **2019**, *141* (46), 18358–18369. https://doi.org/10.1021/jacs.9b07976.
(9) Lee, D. K.; Lee, D.; Lumley, M. A.; Choi, K.-S. Progress on Ternary Oxide-Based Photoanodes for Use in Photoelectrochemical Cells for Solar Water Splitting. *Chem. Soc. Rev.* **2019**, *48* (7), 2126–2157. https://doi.org/10.1039/C8CS00761F.
(10) Siegfried, M. J.; Choi, K.-S. Electrochemical Crystallization of Cuprous Oxide with Systematic Shape Evolution. *Adv. Mater.* **2004**, *16* (19), 1743–1746. https://doi.org/10.1002/adma.200400177.
(11) Sullivan, I.; Zoellner, B.; Maggard, P. A. Copper(I)-Based p-Type Oxides for Photoelectrochemical and Photovoltaic Solar Energy Conversion. *Chem. Mater.* **2016**, *28* (17), 5999–6016. https://doi.org/10.1021/acs.chemmater.6b00926.
(12) Bagal, I. V.; Chodankar, N. R.; Hassan, M. A.; Waseem, A.; Johar, M. A.; Kim, D.-H.; Ryu, S.-W. Cu_2O as an Emerging Photocathode for Solar Water Splitting - A Status Review. *Int. J. Hydrog. Energy* **2019**, *44* (39), 21351–21378. https://doi.org/10.1016/j.ijhydene.2019.06.184.
(13) Li, C.; He, J.; Xiao, Y.; Li, Y.; Delaunay, J.-J. Earth-Abundant Cu-Based Metal Oxide Photocathodes for Photoelectrochemical Water Splitting. *Energy Environ. Sci.* **2020**, *13* (10), 3269–3306. https://doi.org/10.1039/D0EE02397C.
(14) Jang, Y. J.; Lindberg, A. E.; Lumley, M. A.; Choi, K.-S. Photoelectrochemical Nitrogen Reduction to Ammonia on Cupric and Cuprous Oxide Photocathodes. *ACS Energy Lett.* **2020**, *5* (6), 1834–1839. https://doi.org/10.1021/acsenergylett.0c00711.
(15) Schreier, M.; Luo, J.; Gao, P.; Moehl, T.; Mayer, M. T.; Grätzel, M. Covalent Immobilization of a Molecular Catalyst on Cu_2O Photocathodes for CO_2 Reduction. *J. Am. Chem. Soc.* **2016**, *138* (6), 1938–1946. https://doi.org/10.1021/jacs.5b12157.
(16) Paracchino, A.; Laporte, V.; Sivula, K.; Grätzel, M.; Thimsen, E. Highly Active Oxide Photocathode for Photoelectrochemical Water Reduction. *Nat. Mater.* **2011**, *10* (6), 456–461. https://doi.org/10.1038/nmat3017.
(17) Paracchino, A.; Mathews, N.; Hisatomi, T.; Stefik, M.; Tilley, S. D.; Grätzel, M. Ultrathin Films on Copper(i) Oxide Water Splitting Photocathodes: A Study on Performance and Stability. *Energy Environ. Sci.* **2012**, *5* (9), 8673. https://doi.org/10.1039/c2ee22063f.

(18) Steier, L.; Herraiz-Cardona, I.; Gimenez, S.; Fabregat-Santiago, F.; Bisquert, J.; Tilley, S. D.; Grätzel, M. Understanding the Role of Underlayers and Overlayers in Thin Film Hematite Photoanodes. *Adv. Funct. Mater.* **2014**, *24* (48), 7681–7688. https://doi.org/10.1002/adfm.201402742.

(19) Luo, J.; Steier, L.; Son, M.-K.; Schreier, M.; Mayer, M. T.; Grätzel, M. Cu_2O Nanowire Photocathodes for Efficient and Durable Solar Water Splitting. *Nano Lett.* **2016**, *16* (3), 1848–1857. https://doi.org/10.1021/acs.nanolett.5b04929.

(20) Pan, L.; Kim, J. H.; Mayer, M. T.; Son, M.-K.; Ummadisingu, A.; Lee, J. S.; Hagfeldt, A.; Luo, J.; Grätzel, M. Boosting the Performance of Cu_2O Photocathodes for Unassisted Solar Water Splitting Devices. *Nat. Catal.* **2018**, *1* (6), 412–420. https://doi.org/10.1038/s41929-018-0077-6.

(21) Vijselaar, W.; Kunturu, P. P.; Moehl, T.; Tilley, S. D.; Huskens, J. Tandem Cuprous Oxide/Silicon Microwire Hydrogen-Evolving Photocathode with Photovoltage Exceeding 1.3 V. *ACS Energy Lett.* **2019**, *4* (9), 2287–2294. https://doi.org/10.1021/acsenergylett.9b01402.

(22) Dias, P.; Schreier, M.; Tilley, S. D.; Luo, J.; Azevedo, J.; Andrade, L.; Bi, D.; Hagfeldt, A.; Mendes, A.; Grätzel, M.; Mayer, M. T. Transparent Cuprous Oxide Photocathode Enabling a Stacked Tandem Cell for Unbiased Water Splitting. *Adv. Energy Mater.* **2015**, *5* (24), 1501537. https://doi.org/10.1002/aenm.201501537.

(23) Son, M.-K.; Steier, L.; Schreier, M.; Mayer, M. T.; Luo, J.; Grätzel, M. A Copper Nickel Mixed Oxide Hole Selective Layer for Au-Free Transparent Cuprous Oxide Photocathodes. *Energy Environ. Sci.* **2017**, *10* (4), 912–918. https://doi.org/10.1039/C6EE03613A.

(24) Pan, L.; Liu, Y.; Yao, L.; Dan Ren; Sivula, K.; Grätzel, M.; Hagfeldt, A. Cu_2O Photocathodes with Band-Tail States Assisted Hole Transport for Standalone Solar Water Splitting. *Nat. Commun.* **2020**, *11* (1), 318. https://doi.org/10.1038/s41467-019-13987-5.

(25) Kunturu, P. P.; Huskens, J. Efficient Solar Water Splitting Photocathodes Comprising a Copper Oxide Heterostructure Protected by a Thin Carbon Layer. *ACS Appl. Energy Mater.* **2019**, *2* (11), 7850–7860. https://doi.org/10.1021/acsaem.9b01290.

(26) Liu, Y. L.; Liu, Y. C.; Mu, R.; Yang, H.; Shao, C. L.; Zhang, J. Y.; Lu, Y. M.; Shen, D. Z.; Fan, X. W. The Structural and Optical Properties of Cu_2O Films Electrodeposited on Different Substrates. *Semicond. Sci. Technol.* **2005**, *20* (1), 44–49. https://doi.org/10.1088/0268-1242/20/1/007.

(27) Lhermitte, C. R.; Polo, A.; Yao, L.; Boudoire, F. A.; Guijarro, N.; Sivula, K. Generalized Synthesis to Produce Transparent Thin Films of Ternary Metal Oxide Photoelectrodes. *ChemSusChem* **2020**, *n/a* (n/a). https://doi.org/10.1002/cssc.202000926.

(28) Kurniawan, M.; Stich, M.; Marimon, M.; Camargo, M.; Peipmann, R.; Hannappel, T.; Bund, A. Electrodeposition of Cuprous Oxide on a Porous Copper Framework for an Improved Photoelectrochemical Performance. *J. Mater. Sci.* **2021**, *56* (20), 11866–11880. https://doi.org/10.1007/s10853-021-06058-y.

(29) Jin, Z.; Hu, Z.; Yu, J. C.; Wang, J. Room Temperature Synthesis of a Highly Active Cu/Cu_2O Photocathode for Photoelectrochemical Water Splitting. *J. Mater. Chem. A* **2016**, *4* (36), 13736–13741. https://doi.org/10.1039/C6TA05274F.

(30) Li, L.; Liang, J.; Qin, L.; Chen, D.; Huang, Y. *In Situ* Growth of a P-Type CuSCN/Cu_2O Heterojunction to Enhance Charge Transport and Suppress Charge Recombination. *J. Mater. Chem. C* **2019**, *7* (23), 6872–6878. https://doi.org/10.1039/C9TC02147G.

(31) Kim, J.; Lee, Y.; Gil, B.; Yun, A. J.; Kim, J.; Woo, H.; Park, K.; Park, B. A Cu_2O–CuSCN Nanocomposite as a Hole-Transport Material of Perovskite Solar Cells for Enhanced Carrier Transport and Suppressed Interfacial Degradation. *ACS Appl. Energy Mater.* **2020**, *3* (8), 7572–7579. https://doi.org/10.1021/acsaem.0c01001.

(32) Kirfel, A.; Eichhorn, K. Accurate Structure Analysis with Synchrotron Radiation. The Electron Density in Al_2O_3 and Cu_2O. *Acta Crystallogr. A* **1990**, *46* (4), 271–284. https://doi.org/10.1107/S0108767389012596.

(33) Biesinger, M. C. Advanced Analysis of Copper X-Ray Photoelectron Spectra: Advanced Analysis of Copper X-Ray Photoelectron Spectra. *Surf. Interface Anal.* **2017**, *49* (13), 1325–1334. https://doi.org/10.1002/sia.6239.

(34) Murugadoss, G.; Rajesh Kumar, M.; Kuppusami, P. Synthesis of Cu_2O-$Cu(OH)_2$ Nanocomposite from CuSCN Precursor by a Facile Chemical Precipitation Method. *Mater. Lett.* **2021**, *284*, 128866. https://doi.org/10.1016/j.matlet.2020.128866.

(35) Malerba, C.; Biccari, F.; Leonor Azanza Ricardo, C.; D'Incau, M.; Scardi, P.; Mittiga, A. Absorption Coefficient of Bulk and Thin Film Cu_2O. *Sol. Energy Mater. Sol. Cells* **2011**, *95* (10), 2848–2854. https://doi.org/10.1016/j.solmat.2011.05.047.

(36) Tilley, S. D.; Schreier, M.; Azevedo, J.; Stefik, M.; Graetzel, M. Ruthenium Oxide Hydrogen Evolution Catalysis on Composite Cuprous Oxide Water-Splitting Photocathodes. *Adv. Funct. Mater.* **2014**, *24* (3), 303–311. https://doi.org/10.1002/adfm.201301106.